International Journal of Plasticity 171 (2023) 103768

Contents lists available at ScienceDirect

International Journal of Plasticity

journal homepage: www.elsevier.com/locate/ijplas

Element-dependent evolution of chemical short-range ordering tendency of NiCoFeCrMn under irradiation

Yundi Zhou [a], Tan Shi [a,*], Jing Li [a], Lu Wu [b], Qing Peng [c,d,e,*], Chenyang Lu [a,*]

[a] School of Nuclear Science and Technology, Xi'an Jiaotong University, Xi'an, 710049, China
[b] The First Sub-institute, Nuclear Power Institute of China, Chengdu, 610041, China
[c] State Key Laboratory of Nonlinear Mechanics, Institute of Mechanics, Chinese Academy of Sciences, Beijing 100190, China
[d] School of Engineering Sciences, University of Chinese Academy of Sciences, Beijing, 100049, China
[e] Guangdong Aerospace Research Academy, Guangzhou, 511458, China

ARTICLE INFO

Keywords:
High-entropy alloys
Short-range order
Molecular dynamics
Kinetic Monte Carlo
Irradiation damage

ABSTRACT

The evolution of short-range order (SRO) structures under irradiation has a great impact on the mechanical properties of high-entropy alloys. In this study, the atomistic mechanism of the evolution of SRO during and after cascade collisions was investigated in NiCoFeCrMn by multi-scale modeling using molecular dynamics and lattice kinetic Monte Carlo simulations. SRO structures could be destructed by cascade collisions in short time and recovered by atomic diffusion in a much longer time. The destruction rate depends on the primary knock-on atom energies in cascade collisions and shows a universal law with respect to the number of replacement-per-atom. The vacancy diffusion simulations reveal that the SRO recovery rates of different element pairs vary significantly due to the distinct diffusion rates. Consequently, the SRO state under irradiation differs from that in thermodynamic equilibrium due to the difference of destruction and recovery rate for each element pair. The evolution of SRO is a result of the competition between the destruction and recovery mechanisms and depends heavily on the irradiation conditions.

1. Introduction

High-entropy alloys (HEAs) mainly consist of 4 to 5 elements with the concentration of each element varying between 5 and 35 at. % (Yeh et al., 2004). HEAs exhibit outstanding mechanical performance (Feng et al., 2017; Li et al., 2023, 2016; Zhang et al., 2021, 2020b) , radiation tolerance (Granberg et al., 2016; Lu et al., 2016; Li et al., 2021; Zhang et al., 2015), and corrosion resistance (Fu et al., 2021), which makes HEAs a promising class of materials for nuclear applications. In recent years, owing to the interatomic enthalpic interactions among the constituent elements, it has been realized that the elements are unlikely to be totally randomly distributed, especially at lower temperatures (Ding et al., 2018, 2019b; Li et al., 2019b). Recently, the short-range order (SRO) structures in medium-entropy alloys (MEAs) and HEAs have been directly observed by transmission electron microscopy (Chen et al., 2021b, 2022; Su et al., 2022a). SRO affects many aspects of material properties including microstructural deformation mechanisms (Gupta et al., 2022a), dislocation activities (Li et al., 2019b), creep resistance (Sun et al., 2022), diffusion dynamics (Xing et al., 2022), radiation resistance (Liu et al., 2022; Shi et al., 2022; Zhang et al., 2023b) and defect evolution (Shi et al., 2021, 2023a, 2023b). For

* Corresponding authors.
E-mail addresses: tan.shi0122@xjtu.edu.cn (T. Shi), pengqing@imech.ac.cn (Q. Peng), chenylu@xjtu.edu.cn (C. Lu).

https://doi.org/10.1016/j.ijplas.2023.103768
Received 7 May 2023; Received in revised form 17 September 2023;
Available online 5 October 2023

instance, SRO can enhance the ruggedness of the energy landscape, resulting in increase of the dislocation activation barriers (Li et al., 2019b) and localization of point defect diffusion (Xing et al., 2022; Zhao, 2021). The existence of SRO can also delay the growth of radiation-induced defect microstructures, such as dislocation loops (Liu et al., 2022). Moreover, the size of vacancy clusters during defect diffusion can also be impacted by SRO (Shi et al., 2023b). In addition, since the Generation IV reactors will be operated at a wide temperature and dose range (Zinkle and Was, 2013), it is important to understand the evolution of SRO under irradiation due to the significant effects of SRO on defect evolution and mechanical properties.

For alloys with a certain tendency of ordering, two competing processes are involved under irradiation: chemical disordering induced by cascade displacement and chemical ordering induced by thermally-activated atom diffusion (Enrique and Bellon, 2000). The disordering is favored at low irradiation temperatures, but with the increase of temperature, radiation-enhanced ordering, i.e., ordering induced by atomic diffusion enhanced by radiation-induced defects, starts to play a larger role in the overall structural evolution. The competition between these two processes can lead to different steady-state regimes, including solid solution, compositional patterning at different spatial scales, and phase separation (Averback et al., 2021). From the experimental aspect, the evolution of ordering tendency has been studied in various alloys. Disordering of Ni_3Al was observed after Au, I and Al ion irradiation at room temperature. However, the degree of order recovered after thermal annealing (Yoshizaki et al., 2015). With Kr ion irradiation, the ordered Ni_3(Al, Ti) precipitates in Inconel X-750 alloy became completely disordered at 0.06 dpa from 333 K to 673 K, while at temperatures higher than 773 K, the precipitates remained ordered up to 5.4 dpa. This indicated that the thermal reordering of Ni_3(Al, Ti) between 673 K and 773 K could in large part compensate for the radiation-induced disordering (Zhang et al., 2014). In a recent study, Fe-18Cr was irradiated with Fe ions under a wide range of dose rates (10^{-5} - 10^{-3} dpa/s) and temperatures (573 to 723 K) (Zhao et al., 2022). The results showed that the Cr-rich precipitates dissolved only at 300 °C and 10^{-3} dpa/s. Similar irradiation experiments were performed on $AlCoCrFeNi_{2.1}$ HEA, which is composed of B2 phase with NiAl crystal structure. The order degree of the B2 phase reduced after He ion irradiation at a flux of 2.78 ions/cm^2/s at both 298 K and 723 K. The phase-field was used to explain the formation of precipitation in FeCr (Ke et al., 2019) and AgCu (Demange et al., 2017). It was found that Cr-rich α' precipitates are formed under neutron/heavy-ion irradiation at 573 K between 10^{-8} to 10^{-6} dpa/s in FeCr (Ke et al., 2019). Another phase-field study coupled with molecular dynamics shows that the patterning can only be achieved when the cascade is larger than a critical size, which corresponds to irradiation with larger primary knock-on atom (PKA) energies (Demange et al., 2017). It can be concluded from these studies that the irradiation temperature, dose rate and PKA energy have a significant impact on the steady-state structure.

It is reported that the evolution of SRO structure follows similar patterns to the evolution of precipitates in aforementioned alloys under irradiation conditions (Arkoub and Jin, 2023). For HEAs with low mixing enthalpy, small atomic size difference and small electronegativity (Ding et al., 2019a) among the constituent elements, it is difficult to form segregations but SRO structures exist inevitably. Thus, it is important to study the SRO evolution under various irradiation conditions in HEAs. Atomistic simulations have been used to illustrate the dynamics of the SRO disordering and ordering process. The disordering of SRO was studied in both HEAs of CuNiCoFe (Koch et al., 2017) and NiCoFeCrMn (Li et al., 2022) by cascade overlapping simulations. It was shown that when the diffusion-induced recovery of SRO is neglected, for initial structures with and without SRO, the SRO structure can be progressively destroyed or slightly promoted to a weak degree of SRO level, respectively. The ordering process was studied in a model FCC HEA by lattice kinetic Monte Carlo (kMC) simulation using Lennard-Jones potential, showing the strong dependence of the ordering rate on the annealing temperature and time (Shen et al., 2021).

When SRO tuning strategy is attempted to achieve enhanced irradiation resistance, a critical question is whether the initial SRO structure maintains during the long period of neutron irradiation at elevated temperature. Another concern is that as ion irradiation is frequently used to emulate neutron irradiation, the orders of magnitude of difference in dose rate could lead to significantly different SRO evolution tendency due to the longer SRO recovery time in reactor environment. Recent ion irradiation experiment showed that the formation of SRO in NiCoFeCrMn was promoted under 3-MeV Ni^{2+} ion irradiation with a dose rate of 10 dpa/h at a total dose of 50 dpa at 420 °C and 540 °C due to the radiation-enhanced diffusion (Su et al., 2022a). The neutron irradiation experiment of NiFeMnCr at 60 °C also gave hints for the formation of SRO during the period of neutron irradiation (Li et al., 2019a). As SRO significantly impacts the defect evolution and mechanical properties in HEAs, it is important to understand how the degree of SRO varies under irradiation. Regarding the process of cascade-induced SRO destruction, the role of PKA energy, corresponding to different types of incident particles and different spatial scales of atomic mixing, remains to be explored in HEAs. For the process of SRO recovery induced by radiation-enhanced diffusion, it was shown by irradiation experiments and first-principles calculations that in NiCoFeCrMn (Chen et al., 2020; Su et al., 2022b) vacancies dominate the elemental segregation behavior through the inverse Kirkendall effect (Wharry and Was, 2013). However, it is unclear how the differences of diffusion coefficients of the constituent elements affect the SRO recovery tendency. As the HEA properties are dependent on the extent of SRO or structural inhomogeneity, it is also to be answered whether the SRO structure under irradiation can be described by an equivalent thermodynamic equilibrium state without irradiation for the accurate modeling of the material performance under long-term irradiation. Motivated by these questions, atomistic simulations were performed to evaluate the SRO evolution tendency in NiCoFeCrMn.

In this work, the destruction and recovery of SRO in equiatomic NiCoFeCrMn were studied by a multiscale method. where the displacement cascade process is simulated through molecular dynamics (MD) (Peng et al., 2018) and the atomistic diffusion is modelled via kMC simulations. First, the SRO structures were constructed by a hybrid MC + MD method at various temperatures. Next, cascade overlapping simulations were performed to study the process of SRO destruction with different PKA energies over a wide range of SRO levels. The SRO recovery mechanism was then studied through lattice kMC simulation to investigate the SRO formation by vacancy-mediated atomic diffusion. We showed that the SRO evolution under irradiation is element-dependent and differs from that in thermodynamic equilibrium conditions. The competition between the disordering and ordering mechanism and the steady-state SRO structures under different irradiation conditions were also discussed.

2. Method

In our multiscale model, the atomistic structures, thermodynamics, short-term displacement cascade process of equiatomic NiCoFeCrMn are modeled by means of molecular dynamic simulations. The long-term recovering process based on vacancy-mediated atomic diffusion is modeled by means of kinetic Monte Carlo method. In addition, the SRO structures are generated by a hybrid MC + MD method.

2.1. Interatomic potential

For MD simulations, the atomic interactions of NiCoFeCrMn was described by the potential of 2-nn modified embedded atom method (Choi et al., 2018). The cohesive energy, lattice constant, phase structures, surface energy, elastic constants, vacancy formation energy and migration energy of unitary subsystems were considered. The mixing enthalpy and planar defect energy were also included in the development of the alloy potential (Choi et al., 2018). The interstitial formation energy of unary subsystems and cohesive energy of binary alloys were verified by comparing these properties with first-principles results (see Table S1 and S2 of Supplementary Material), showing relatively good agreement for the relative order of interstitial formation energy and binary mixing enthalpy. The Ziegler-Biersack-Littmark (ZBL) potential (Ziegler and Biersack, 1985) was also incorporated in the potential to describe the atomic interactions at short range during collision cascades.

2.2. SRO parameter

The Warren–Cowley SRO parameters α_n^{ij} were used to quantify the chemical ordering (Cowley, 1960):

$$\alpha_n^{ij} = 1 - \frac{P_n^{ij}}{c_j}, \tag{1}$$

where n refers to the n^{th} nearest-neighbor of the reference atom, P_n^{ij} represents the average probability to find type j atom around type i atom in the n^{th} neighboring shell, c_j is the average concentration of atom type j in the alloy. A positive α_n^{ij} indicates segregation between atom type i and j whereas a negative value indicates tendency of clustering. To further measure the chemical ordering of the system, a global SRO parameter was proposed:

$$\alpha = \frac{1}{N}\sum_{j,j\geq i}\sum_{i}|\alpha_n^{ij}|, \tag{2}$$

where N is the total number of element pairs, which equals to 15 in the studied alloy. A large α represents a strong SRO level of the entire structure.

2.3. Thermodynamic equilibrium conditions

In this study, all the atomistic simulations were performed using the LAMMPS code (Plimpton, 1995). To obtain the different degrees of SRO, the hybrid MC + MD method was used to establish the thermodynamic equilibrium states of NiCoFeCrMn at various annealing temperatures ranging from 300 K to 1200 K under canonical ensemble. For the MD step, the Nosé-Hoover thermostat was applied with NPT ensemble with a timestep of 2.5 fs. The MC step was invoked every 25 MD steps with 1000 swap attempts of atom pairs in each MC step. The simulation was stopped when the potential energy variation per atom within the last 100 MC steps was less than 1×10^{-3} eV/atom. A simulation box annealed at 300 K with 55,296 atoms ($24 \times 24 \times 24$ unit cells) was prepared for the subsequent cascade overlapping simulations.

2.4. Cascade overlapping simulations

Cascade overlapping simulations were performed with PKA energies of 0.5, 2, and 5 keV. Initial structures of random solid solution and SRO annealed at 300 K were both studied. A random atom was selected as the PKA and a recoil direction of ⟨135⟩ was chosen to avoid channeling effect (Gao et al., 1996). In the cascade stage, the simulation was performed under NVE ensemble. An adaptive timestep was used to restrict the maximal displacement of atoms within 0.02 Å and the maximal timestep below 1 fs. Each recoil event lasted for about 3, 13, and 26 ps for PKA energies of 0.5, 2, and 5 keV, respectively, which is sufficient for the system to equilibrate. The dpa rate and the temperature considered in the cascade overlapping simulations are about 10^7 dpa/s and 300 K, respectively. After the cascade stage, the NVT ensemble was applied to remove the extra energy introduced by the PKA. Several thousands of recoil events were simulated to reach a dose level of 0.7 dpa according to the NRT displacement model (Norgett et al., 1975). A threshold displacement energy of 40 eV was used for all elements (Levo et al., 2017; Li et al., 2022).

The open-source program OVITO was used for visualization and structural analysis (Stukowski, 2010). The Wigner-Seitz method (Stukowski, 2012) was adopted to recognize the interstitials and vacancies. The cutoff distance to distinguish two separate interstitial or vacancy clusters was set to 4 Å. The common neighbor analysis method was used to define the defect region and the matrix region. Only the atoms within the FCC configuration were considered to be in the matrix, whereas all the structures other than the FCC

structure were considered as defects.

2.5. Kinetic Monte Carlo simulations

For the SRO formation kinetics, we assume that the SRO recovery is dominated by the vacancy migration (Butler, 2006; Shen et al., 2021). An atomic model composed of 2047 atoms and a monovacancy was used in the simulation. A KMC event was defined as a vacancy jump to one of the twelve nearest-neighbor sites. The Arrhenius equation was used to estimate the jump rate k_i for neighboring site i:

$$k_i = v_0 exp\left(-\frac{\Delta E}{k_B T}\right), \tag{3}$$

where an attempt frequency (v_0) of 10^{13} s^{-1} is taken as the typical atomic vibrational frequency (Sickafus et al., 2007). k_B is the Boltzmann constant and ΔE is the migration barrier and ΔE is the migration barrier, which is defined as:

$$\Delta E = E_s - E_0, \tag{4}$$

where E_0 is the total energy of the structure before migration and E_s is the saddle-point energy. In this study, the saddle structure energy was approximated by the middle-point energy. This method was validated by comparing with the NEB method (see Fig. S1 of Supplementary Materials) and has also been adopted to calculate the migration energy of FCC HEA (Zhao et al., 2018). The time interval of each kMC step was computed as:

$$t = -\frac{1}{\sum_{i=1}^{n} k_i \, In(s)}, \tag{5}$$

where n is the number of neighbor sites, s is a random number ranging from 0 to 1 and i is the index of all possible migration events.

3. Results

3.1. SRO at equilibrium state

Fig. 1(a) to (d) show four (300, 600, 900, 1200 K) representative thermodynamic equilibrium states of NiCoFeCrMn from 300 K and 1200 K, respectively. The SRO tendency is weaker at higher annealing temperatures. However, there is a clear clustering of Cr-Cr pairs at low annealing temperature. In addition, Mn atoms tend to be located within or around Cr-rich region, whereas Co and Fe atoms tend to be grouped together and away from the Cr-rich region. The evolution of the magnitude of the first nearest-neighbor (1nn) SRO parameters with annealing temperatures is shown in Fig. 1(e). Consistent with Fig. 1(a) to (d), the strongest affinity corresponds to Cr-

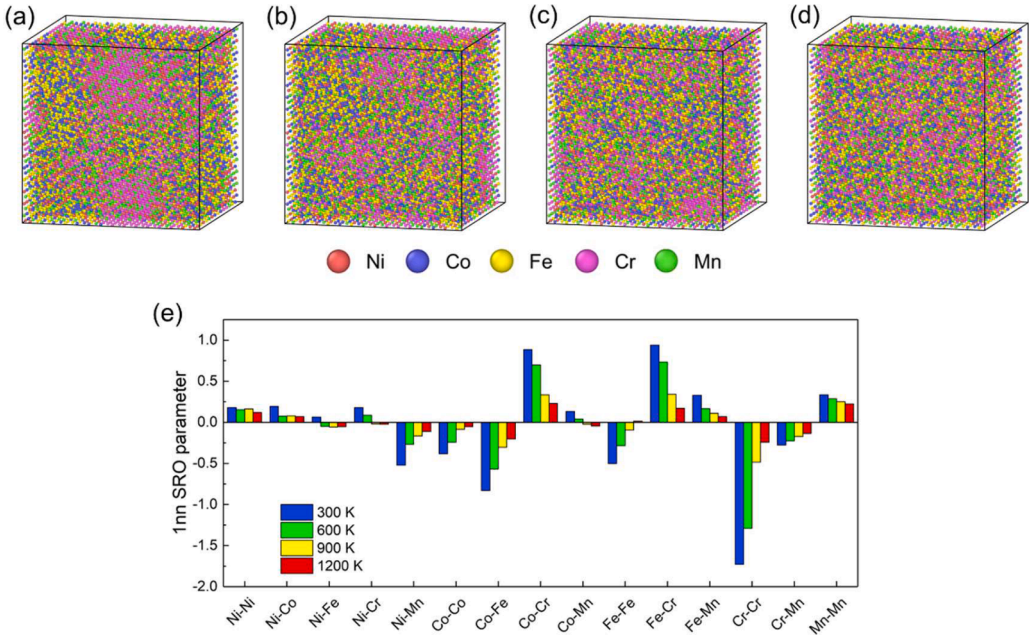

Fig. 1. Atomistic structures of NiCoFeCrMn annealed at (a) 300 K, (b) 600 K, (c) 900 K and (d) 1200 K. (e) First nearest-neighbor SRO parameters of different element pairs at annealing temperatures of 300 K - 1200 K.

Cr pair, followed by Co-Fe, Ni-Mn and Fe-Fe. In contrast, Co-Cr and Fe-Cr neighbors are not preferred. The ordering tendencies are consistent with experimental results of preferential formation of local regions enriched in Cr-Cr, Co-Fe and Ni-Mn after long-term annealing in NiCoFeCrMn (Otto et al., 2016). The expected trend of increasing SRO level with the decrease of temperature was also observed. At higher temperatures, the contribution of configurational entropy outweighs the mixing enthalpy, whereas at low temperatures the mixing enthalpy dominates the system free energy and leads to chemical ordering. Previous study suggested that the ordering tendency of different element pairs can be explained by the chemical affinity and exclusivity of the composition in forming atomic pairs (Chen et al., 2021a). For binary subsystems in NiCoFeCrMn, the cohesive energy of AB_3 $L1_2$ structure was calculated (see Table S2), showing good qualitative agreement with first-principles results (Chen et al., 2021a). However, a strong correlation was not observed between the cohesive energies of ordered binary alloys and NiCoFeCrMn, which may be attributed to the differences in chemical environment induced by chemical complexity and chemical disorder.

3.2. SRO destruction

To study the SRO destruction process, the cascade overlapping simulations were performed with two different initial structures: a structure of random solid solution and an SRO structure annealed at 300 K (S300). The SRO evolution trends for these two initial conditions are presented in Fig. 2(a-c). Only the atoms in the perfect FCC matrix were included in the SRO analysis and the atoms in irradiation defects were excluded. It is found that the initial structure has limited impact on the converged chemical ordering level, as shown in Fig. 2(d). For S300, the SRO structure is destroyed progressively during the overlapping cascades and decays to a weak degree of ordering. For the structure of random solid solution, the SRO parameters of different element pairs converge to approximately the same level as the case of S300. It is worth noting that due to the high dose rate of simulations, the long-term defect diffusion is not considered. Thus, the SRO destruction process studied by the approach of cascade overlapping is under the condition of negligible SRO recovery, corresponding to irradiation conditions at low temperature. For the current study of ordering/disordering in the matrix, cascade overlapping simulations can be regarded as an effective method to obtain SRO destruction rate over a wide range of SRO levels.

To study the impact of PKA energy on the SRO destruction process, cascade overlapping simulations with PKA energies of 0.5, 2, and 5 keV were performed with an initial structure of S300. The evolution of global SRO parameter as a function of irradiation dose is shown in Fig. 3(a), where the dose was calculated according to the NRT model (Norgett et al., 1975). With the increase of PKA energy, the destruction of SRO appears to be faster. However, although the NRT model is widely used to determine the irradiation dose for

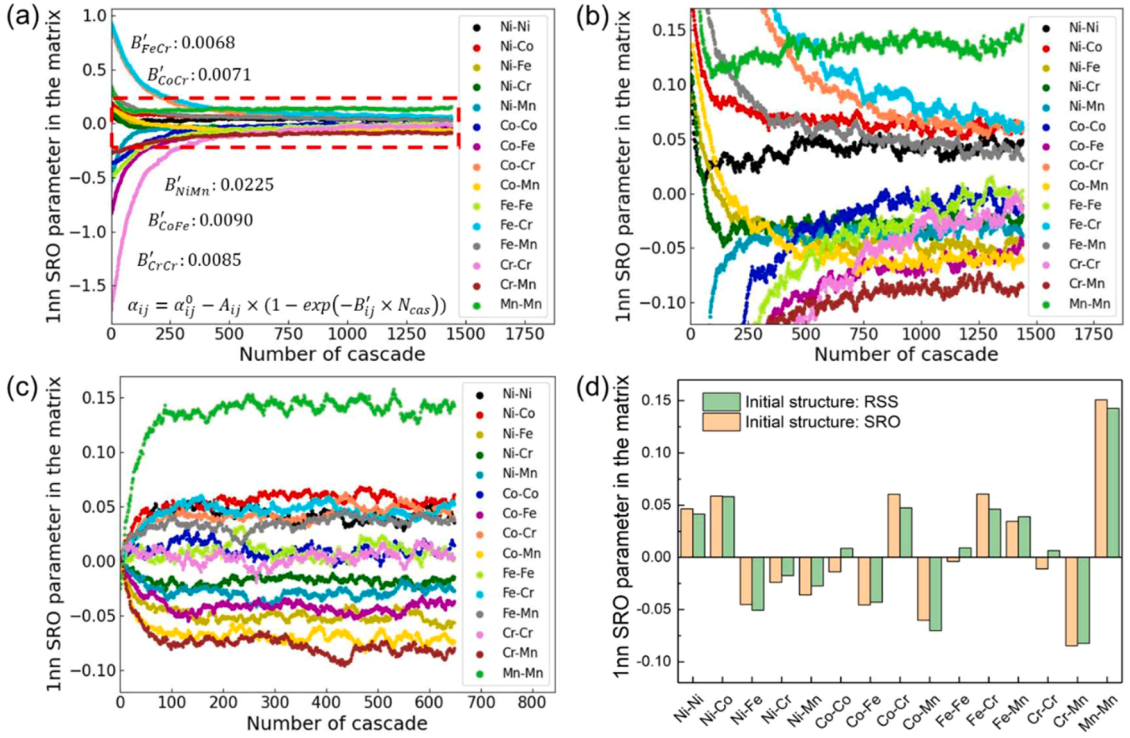

Fig. 2. SRO evolution with initial structures of (a-b) S300 and (c) random solid solution as a function of the number of cascade in cascade overlapping simulations with a PKA energy of 5 keV. The B'_{ij} parameters are shown for Fe-Cr, Co-Cr, Co-Fe and Cr-Cr. The red dashed rectangle in (a) is magnified in (b). (d) Comparison of the converged SRO levels from cascade overlapping simulations between initial structures of random solid solution and short-range order.

nuclear materials, it overestimates the number of stable defects and underestimates the number of atom replacement in MD simulations, i.e., the number of atoms that are permanently displaced to replace atoms in other lattice sites (Nordlund et al., 2018). Thus, the replacements-per-atom (rpa) model is adopted as a more appropriate measure of the simulated irradiation dose since it represents the actual atomic mixing in simulations. The replaced atoms are the atoms whose movement exceeds one half of the first nearest-neighbor distance before and after a cascade.

The number of replaced atoms per cascade with different PKA energies is shown in Fig. 3(b). The number of replacements is larger than the number of displacements from the NRT model. The SRO destruction curves of different PKA energies scaled by rpa are highly overlapped (see Fig. 3(c)), showing the strong correlation between the SRO destruction rate and the actual number of atom replacement in simulations. An extra simulation with a higher PKA energy of 20 keV was performed using a larger simulation cell and the SRO destruction trend also coincides with those of lower PKA energies (see Fig. S2). The relocated distance distribution shown in Fig. 3(c) reflects the maximum atomic displacement of each replaced atom. The two clear peaks at ~ 2.5 Å and 3.6 Å correspond to the first and second nearest-neighbor distance in the NiCoFeCrMn lattice. At farther distances, the distribution exhibits an exponential decay with increasing relocated distance, which is consistent with the trend from previous research in AgCu alloy (Demange et al., 2017). Although higher PKA energy leads to a larger cascade volume with more violent atomic arrangement and larger relocated distance, we show here that the SRO destruction rate is mostly determined by the number of rpa from the collision regardless of the PKA energy, showing a straightforward approach to convert the SRO destruction rate under different irradiation conditions.

Here, the relation between SRO parameter and rpa follows an exponential decay:

$$\alpha(rpa) = \alpha_0 - A \times (1 - exp(-B \times rpa)), \tag{6}$$

where α_0 is the initial equilibrium SRO state, A is the SRO difference between the initial state and the final converged state, and B is a fitting parameter that represents the decay constant. In order to provide a set of fitting parameters that can be applied to various PKA energies in NiCoFeCrMn, fitting was performed with the data of all three PKA energies, as shown in Fig. 3(d), where α_0, A and B are 0.49, 0.43 and 0.30, respectively. The good agreement with first-order kinetics indicates that the proportion of SRO structure destroyed per rpa is close to a constant regardless of the PKA energy. However, the decay constants differ for different atom pairs. Fig. 2 (a) lists the decay constants of five element pairs that have the strongest chemical affinity and exclusivity tendency. We note that for the same PKA energy, the rpa is proportional to the number of cascades; therefore, the ratios among decay constants of different

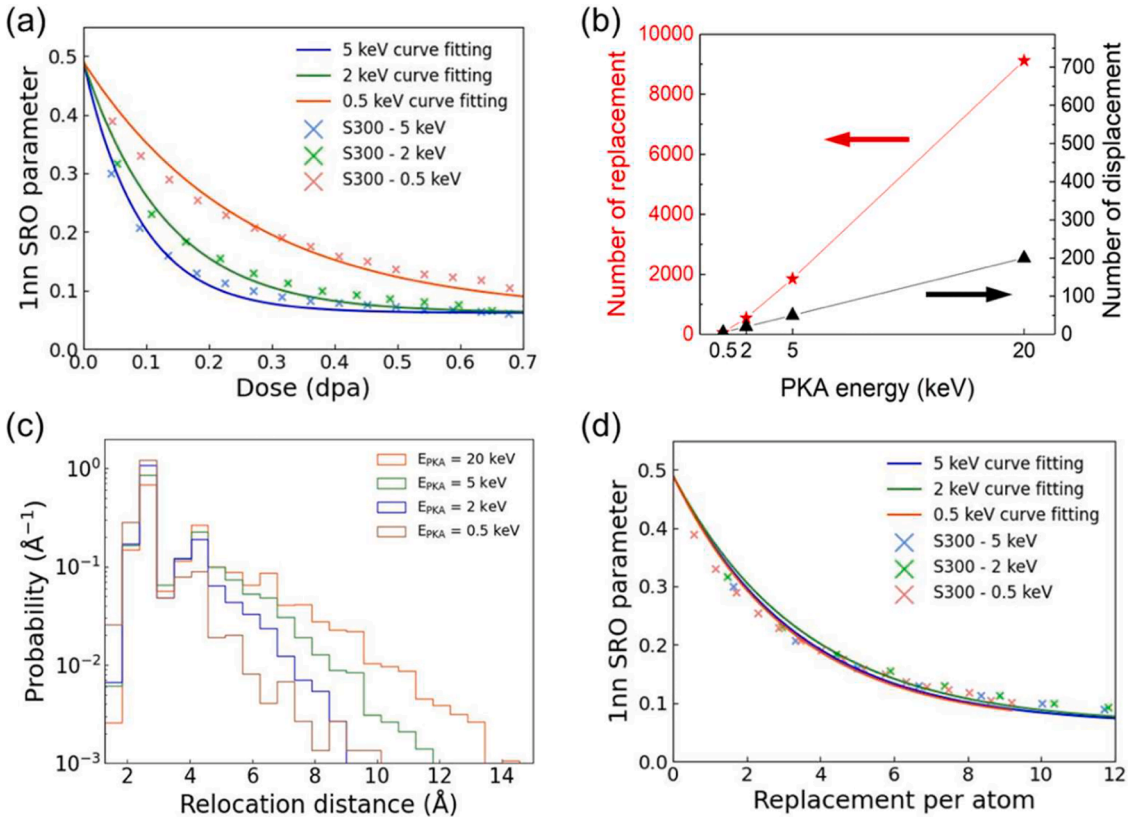

Fig. 3. (a) Evolution of the global SRO parameter as a function of the dpa calculated by the NRT model. (b) The average number of atom replacement and displacement in a single cascade as a function of PKA energy. (c) Relocated distance distribution with various PKA energies. (d) Evolution of the global SRO parameter as a function of the replacement-per-atom (rpa).

element pairs remain the same using the number of cascades, as shown in Fig. 2(a). Among these five element pairs, Fe-Cr and Co-Cr have the lowest decay constants, indicating that they have a slow destruction rate relative to their initial SRO states. The decay constants of Co-Fe and Cr-Cr are slightly larger and that of Ni-Mn pair is the largest, which is approximately three times the values of Fe-Cr and Co-Cr. It can be seen that the relative change of SRO has a strong dependence on the types of element pairs due to the difference in pairwise interactions and energy stability during the non-equilibrium process of thermal spike and the subsequent quenching stage.

A high density of irradiation defects can also impact the evolution of SRO structure in the matrix due to the elemental segregation within and around the defects. Fig. 4 shows the saturated number and concentration of Frenkel pairs as a function of PKA energy. Under the condition that the defect mobility is suppressed, when the PKA energy is higher, the saturation defect concentration becomes lower. This is because the ratio of melting volume of high PKA energy to low PKA energy is larger than the corresponding ratio of defect production, facilitating defect recombination (Boleininger et al., 2023). The defect structures at defect saturation stage with a PKA energy of 5 keV are shown in Fig. 5(a), including defect clusters, 1/6<112> Shockley partial dislocations, as well as stacking fault tetrahedra that consist of 1/6<110> stair-rod dislocations, where defect clusters refer to both vacancy and interstitial-type defects that cannot be categorized as dislocations. No phase transition was observed during irradiation. Most defects are in the form of isolated point defects. The relative proportion of clusters is lower when the cluster size is larger (see Fig. 5(b)), noting that only interstitial clusters are included and vacancy clusters follow a similar trend. The size distribution of interstitial-type defects remains almost the same since the beginning of the cascade overlapping simulation. The analysis of the saturated defect structures at different PKA energies shows that the PKA energy has little effect on the types of defect structures and the cluster size distribution. Although the saturated defect concentrations of different PKA energies differ by a factor of three, the evolution of SRO shows a universal behavior with respect to rpa (see Fig. 3(d)). It shows that with the assumption of negligible defect diffusion, the variation of defect density has a minor impact on the evolution of SRO parameters during the SRO destruction process.

To study the impact of element segregation in defects on the SRO in matrix, a hybrid MC + MD simulation was performed with pre-existing defects in the structure at defect saturation stage with 5-keV PKAs at 600 K. Table 1 lists the composition change in all the defects before and after annealing and Fig. 6(a) shows the snapshot of a representative defect of stacking-fault tetrahedron. Before annealing, defects tend to be depleted in Ni and enriched in Cr and Mn. After annealing, the concentration of Ni and the concentrations of Cr and Mn are further reduced and increased, respectively. In addition, the concentration of Fe changes from the stoichiometric ratio to 11.7 %, and that of Co is reduced to 16.2 %. It indicates that defects have preferred elemental compositions from an energy perspective. Fig. 6(b) shows the 1nn SRO parameters after annealing for initial structures with and without existing defects. Most of the element pairs experience a slight decrease of SRO due to the compositional change in the defects, especially those of strong SRO levels, such as Co-Co, Fe-Cr, Co-Cr and Co-Fe. Although the concentrations of Fe and Co both increase in the matrix, their clustering tendency decreases, showing the complex dependence between SRO and the overall matrix composition. Note that this study only simulates the segregation trend within defects, whereas the influence of element segregation induced by defect-mediated atom diffusion, such as the inverse Kirkendall effect (Wharry and Was, 2013), is not included. The element segregation can impact the region around defects up to 3–4 nm from defect cores (Su et al., 2022b) and is mostly determined by the element-dependent migration energies of vacancies and interstitials. Therefore, to accurately evaluate the impact of defect segregation on SRO, it is necessary to consider the compositional change within and around the defects and the kinetic driving force from irradiation-induced defects. Nevertheless, we show that with a high density of defects within the simulated structure, the impact to the SRO in the matrix is moderate.

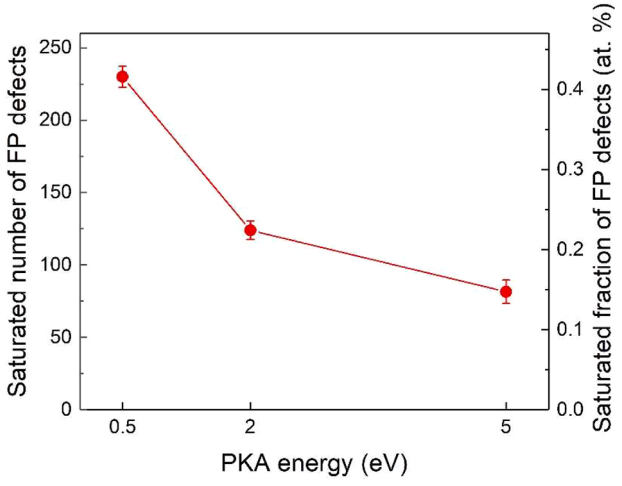

Fig. 4. Saturated number (left y axis) and fraction (right y axis) of Frenkel pairs as a function of PKA energy.

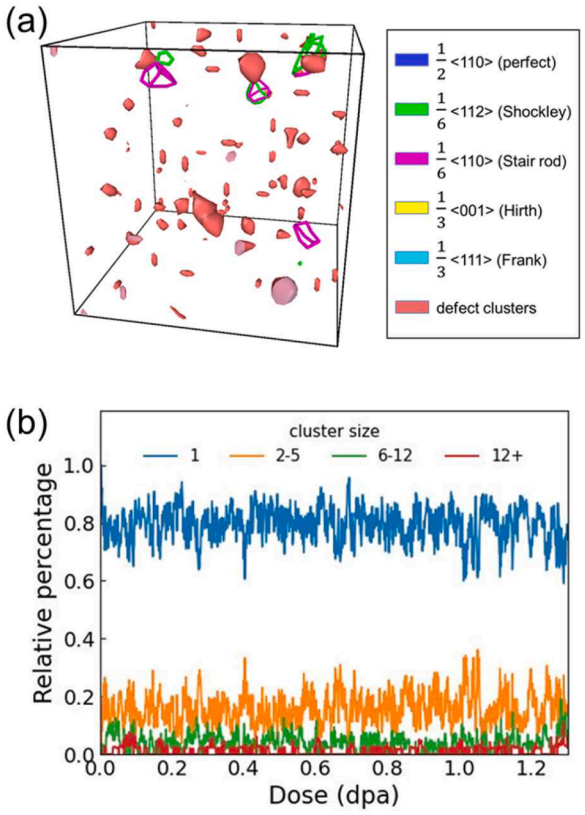

Fig. 5. (a) Snapshot of defect configuration at defect saturation stage with 5-keV PKAs. Atoms in perfect lattice are not shown. Green lines correspond to 1/6<112> partial dislocations, purple lines represent 1/6<110> stair rod dislocations, and red surfaces enclose small defect clusters that cannot be classified as dislocations. (b) Relative percentage of the number of interstitials in interstitial clusters of different sizes as a function of irradiation dose at a PKA energy of 5 keV.

Table 1
Composition in defects before and after annealing with a structure with pre-existing defects at 600 K.

Element	Composition after irradiation (%)	Composition after annealing (%)
Ni	14.4 %	11.3 %
Co	19.5 %	16.2 %
Fe	20.8 %	11.7 %
Cr	22.0 %	32.1 %
Mn	23.3 %	28.7 %

3.3. SRO recovery

Using kinetic Monte Carlo simulations, we have investigated the SRO recovery process by considering the atomistic diffusion at a given temperature. It is worth noting that with the KMC method, we have focused on the effect of vacancy diffusion on the kinetics of SRO formation of different atom pairs in a non-equilibrium structure. This is different from the construction of the equilibrium SRO state, which is achieved using the common approach of hybrid MC + MD, as described in Section 2.2. The results of SRO recovery process are shown in Fig. 7. SRO recovery rates of all element pairs slow down as the SRO level increases. Here, the SRO recovery of Ni-Mn, Co-Fe, Co-Cr, Fe-Cr and Cr-Cr are shown, since they show the strongest SRO tendency. The SRO recovery process at 873 K is illustrated in Fig. 7(a) and the result is an average over three individual simulations. The SRO parameters of Ni-Mn have reached the thermodynamic equilibrium state while SRO parameters of the rest four pairs have not been convergent yet. For the simulation at 573 K, all five element pairs are not recovered to the thermodynamic equilibrium state at the moment shown in Fig. 7(b). The SRO formation rate follows a first-order kinetics (Ziya et al., 2003) and therefore an exponential expression is used to describe the SRO recovery for each element pair. In general, the higher the degree of equilibrium SRO state, the higher the SRO recovery rate. but different elements have different rate constants, which indicates that the recovery rate is element-dependent and is not entirely determined by the degree of equilibrium state.

Fig. 8 shows the detailed process of the SRO recovery at 873 K, including migration barrier, barrier distribution, effective migration

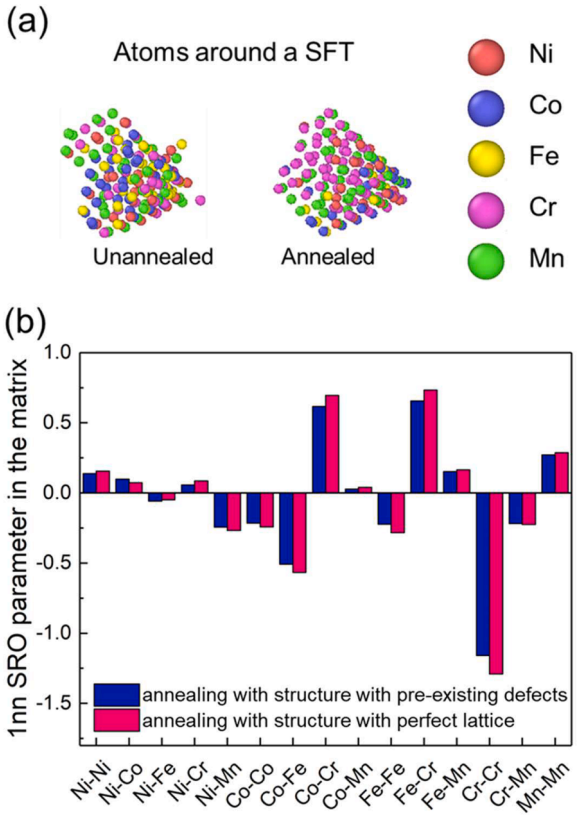

Fig. 6. (a) Local element distribution of a representative stacking fault tetrahedron before and after annealing. (b) Comparison of 1nn SRO parameters in the matrix after MC + MD simulation for structure with pre-existing defects generated from cascade overlapping simulations and for structure of perfect lattice.

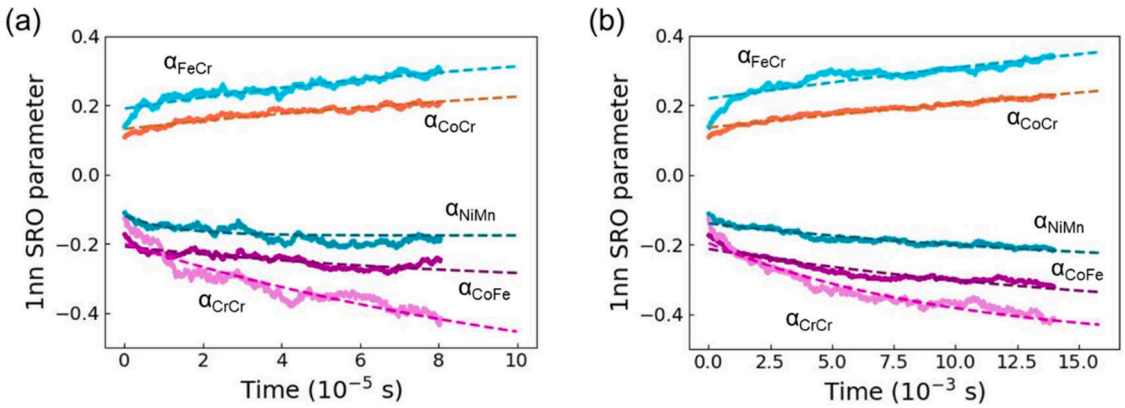

Fig. 7. The SRO recovery trend of Ni-Mn, Co-Fe, Co-Cr, Fe-Cr and Cr-Cr as a function of simulation time at (a) 873 K and (b) 573 K in NiCoFeCrMn in KMC simulations of vacancy diffusion. The exponential fittings to the SRO parameter evolution are represented by dashed curves.

fraction, and pair-wise SRO parameters. It should be noted that the migrations of vacancy trapped in a set of local configurations separated by very low energy barriers without yielding long-range diffusion are only considered once in the effective migration events shown in Fig. 8(a). Fig. 8(a) indicates the difference between the migration barriers of all possible migration events (E_m^{all}) and events that effectively take place (E_m^{eff}). Due to the wide distribution of migration energy, migration events with lower barriers are more likely to occur. The migration barrier distribution of all possible migration events for each element is displayed in Fig. 8(b). Mn has the lowest barrier among the five elements. The order of average migration energy is Co > Ni > Cr > Fe > Mn, which corresponds to the order of the diffusion coefficient of each element in NiCoFeCrMn (Tsai et al., 2013).

The effective migration fraction of different elements is illustrated in Fig. 8(c). Most of the effective migrations are dominated

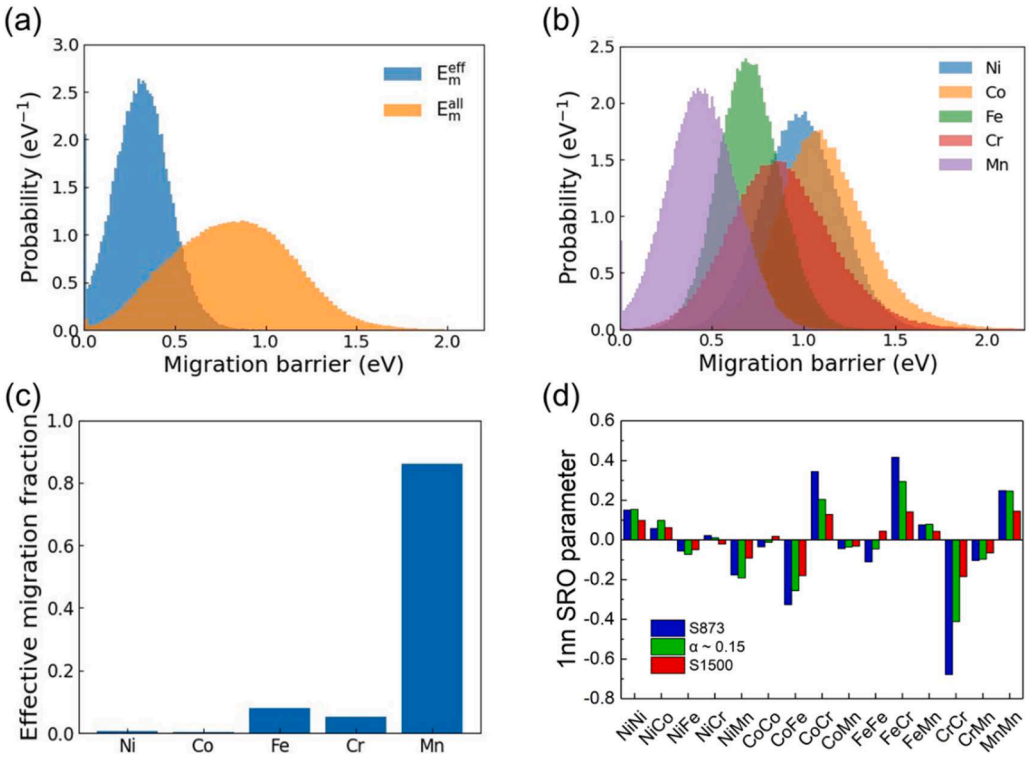

Fig. 8. (a) The migration barrier distribution of all the sampled migration paths (orange) and the events that effectively occur in kMC simulations (blue) at 873 K. (b) The migration barrier distribution of each element based on all the sampled migration paths. (c) The effective migration fraction of different elements during kMC simulations. (d) The SRO parameters of different element pairs at equilibrium states of 873 K (S873), 1500 K (S1500) and at an intermediate transient state from kMC simulations (green).

through Mn, only 5 %−10 % are dominated by Fe and Cr. By comparing the result of 573 K (see Fig. S3 of Supplementary Material) and 873 K, the barrier of effective migration at 573 K is lower than that at 873 K. Accordingly, the Mn fraction during diffusion at 573 K is also higher than that at 873 K. This makes the migration of elements with high migration barriers more difficult at lower temperatures. When it comes to the SRO recovery of each element pair, the Mn-related SRO parameters are almost convergent to the equilibrium state of 873 K. However, SRO parameters of Co-Cr, Fe-Cr and Cr-Cr pairs are far from convergence, as shown in Fig. 8(d). In order to

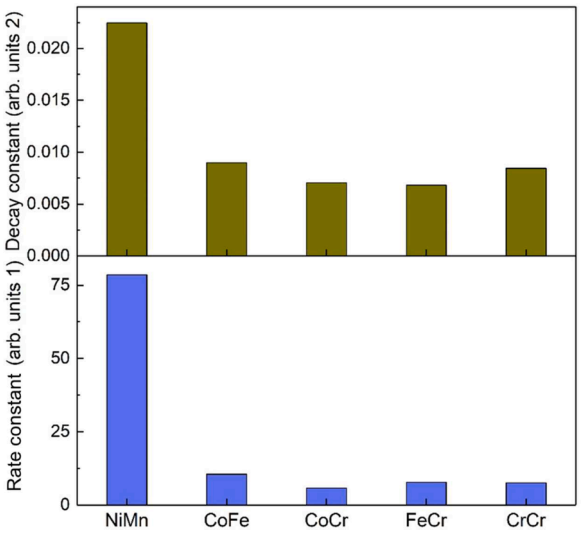

Fig. 9. Comparison of the rate constants in the SRO destruction (upper) and recovery (lower) process for five element pairs that have the most pronounced SRO degrees.

explore the relation between the elemental diffusion coefficient and related SRO structure recovery rate, MD simulations of vacancy-mediated element diffusion were performed at 873 K with the initial structure annealed at 1500 K. The relative diffusion coefficient of each composition is shown in Fig. S4 in Supplementary Information. Taking Mn as a reference, the diffusion coefficient of Fe is 30 % of Mn, followed by Cr, which is about 12 % of Mn. The diffusion coefficients of Ni and Co are extremely low when compared to Mn. As expected, the order of the diffusion coefficient is consistent with the distribution of the migration barrier of various elements. There is a general tendency of higher recovery rate constants for SRO element pairs containing fast-diffusing species, such as those containing Mn. However, there is no quantitative correlation between the recovery rate constant and the diffusion coefficients of the two constituent elements. For instance, Ni has the second slowest diffusion coefficient, but Ni-Mn neighbor has the highest recovery rate, indicating that preference of enthalpic interactions plays an important role in addition to the kinetic driving force.

4. Discussion

The degree of SRO is a dynamic result of the competition of cascade-induced disordering and diffusion-induced ordering in alloy under irradiation. After long-term irradiation, the microstructure in the material will reach a steady state. Previous study proposed that the steady-state configuration of an alloy under irradiation at temperature T is equivalent to the configuration of an unirradiated alloy at temperature T_{eff} (Martin, 1984). The law of corresponding states was used to describe the equivalence relationship:

$$T_{\text{eff}} = T(1+\Delta), \tag{7}$$

where T_{eff} is the effective temperature of the system without irradiation and $\triangle$ is a scale factor, which is related to the diffusion coefficient caused by ballistic mixing and thermally-activated diffusion. However, we found that this equivalence is ineffective in HEAs. Due to the large number of compositions in HEAs, the configuration can be adjusted with a large degree of freedom. Fig. 9 shows the difference of rate constants in SRO destruction and recovery process. For the SRO destruction process, Ni-Mn pair has the highest decay constant, which is about three times as much as the rest of the element pairs. However, for the recovery process, the rate constant of Ni-Mn pair is an order of magnitude larger than those of other element pairs. This is partly due to the fast diffusion of Mn through vacancy. Meanwhile, the high stability of Ni-Mn SRO structure in equilibrium state is another reason. Due to the difference in rate constants of destruction process and recovery process, the SRO state under continuous irradiation may deviate significantly from the thermodynamic equilibrium state at a certain temperature.

Here, two representative irradiation conditions were selected to illustrate the element-dependent SRO evolution, as shown in Fig. 10. The dose rate of the first condition is 10^{-8} dpa/s, which is approximately the dose rate of a typical nuclear reactor. For the second condition, the dose rate is 10^{-3} dpa/s, which is within the range of dose rate under ion irradiation using accelerators. The initial structure is the thermodynamic equilibrium state at 1100 K and the irradiation temperature is assumed to be 573 K for both conditions. In Fig. 10, the upper dashed line is the highly disordered state under extremely high dose rate irradiation. The Warren–Cowley SRO parameter for such condition is not exactly zero because weak local ordering will be preserved as shown from the results in Fig. 2. $\Delta\alpha_{NiMn}$ and $\Delta\alpha_{CrCr}$ correspond to the decrease of SRO induced by a single cascade for element pairs of Ni-Mn and Cr-Cr, respectively. Δt is the average time interval between two cascades. The steady-state SRO level under irradiation was estimated according to the equality between the SRO destruction rate and recovery rate. Based on the SRO destruction rate per dpa at a given SRO state from cascade overlapping simulations and the assumed dpa rate, the SRO destruction rate per time was determined. Regarding the SRO recovery rate, the steady-state vacancy concentrations were estimated based on the rate theory results (Was, 2016; Kozlov, 2009), and the SRO recovery rate was then scaled based on the ratio of assumed steady-state vacancy concentration to the concentration used in the simulation. We mainly focus on Ni-Mn and Cr-Cr pairs for the comparison of SRO evolution, since they show the strongest clustering tendency and significant difference in rate constant. Under typical neutron irradiation condition in reactor (Fig. 10(a)), the SRO structures of Ni-Mn form rapidly at the early stage of irradiation due to the fast diffusion of Mn, but the SRO structures of Cr-Cr form slowly. After long-term evolution, due to the low efficiency of SRO destruction caused by the low neutron dose rate, both Ni-Mn and Cr-Cr can reach their equilibrium SRO state although the time required varies. However, under typical ion irradiation condition (see Fig. 10(b)), although the SRO structure of Ni-Mn is still reserved, the SRO structure of Cr-Cr may be far away from the thermodynamic equilibrium state. It can be concluded that, in contrast to Ni-Mn, the evolution of SRO structure of Cr-Cr is slower, and it is more difficult for the SRO structure of Cr-Cr to be preserved at thermodynamic equilibrium state.

In a recent study, NiMn nanoprecipitates were found in NiFeCrMn after being irradiated with 6 MeV Fe^{3+} ions using a dose rate of 10^{-4} dpa/s at 500 °C (Kamboj and Marquis, 2022). However, no phase decomposition was reported in the ion irradiation studies with higher dose rate on NiFeCrMn with Ni ions using a dose rate of 2×10^{-4} - 2×10^{-3} dpa/s at 25–700 °C (Kumar et al., 2016) and NiCoFeCrMn with Ni ions using a dose rate of 2×10^{-3} dpa/s at 420–580 °C (Lu et al., 2017). Under the aforementioned irradiation conditions, the ordering tendency of Ni-Mn pair is larger at a lower dose rate, which is qualitatively consistent with the SRO evolution trend described in Fig. 10(b). This phase decomposition results reflect the role of irradiation conditions, especially the dose rate, on the microstructure evolution in HEAs under irradiation.

The degree of SRO in HEAs can be tailored by different heat treatment processes (Du et al., 2022; Zhang et al., 2020a). However, the SRO may continue to evolve under long-term reactor irradiation. Due to the relatively low dose rate of neutron irradiation, it may take a long time to reach the steady-state of SRO. The initial structure may impact the performance of HEAs over a long period of time. Many studies emulated the irradiation response of the structure of SRO in HEAs under neutron radiation through ion irradiation. However, the evolution rate of the SRO structure may vary greatly due to the large difference in the dose rates of ion and neutron irradiation. The SRO result of ion irradiation may not represent the average level of SRO evolution under irradiation in reactors. Since the state of the

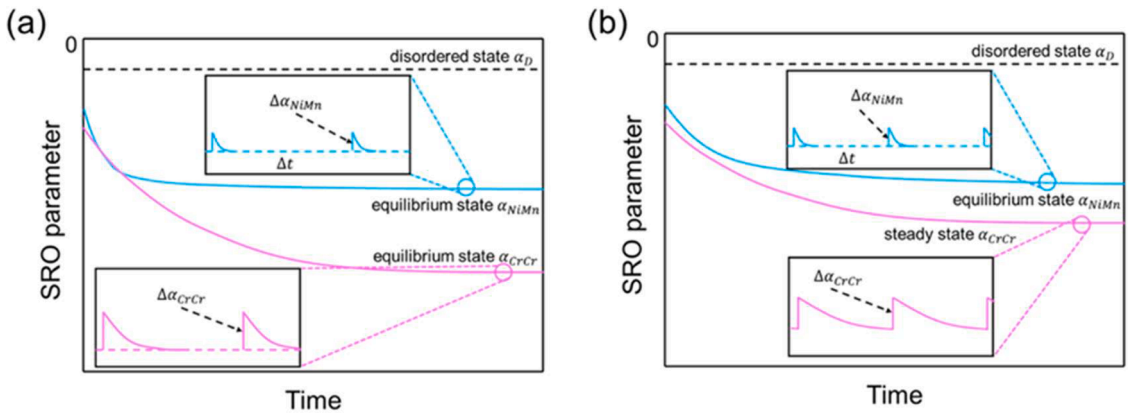

Fig. 10. Schematic evolution of SRO under the continuous competition of destruction and recovery. The following conditions are assumed for this qualitative estimation: (a) the initial structure is annealed at 1100 K, the irradiation dose rate is 10^{-8} dpa/s, the steady vacancy concentration is 10^{-8}. (b) the initial structure is annealed at 1100 K, the irradiation dose rate is 10^{-3} dpa/s, the steady vacancy concentration is 10^{-5}. The irradiation temperature is 573 K for both scenarios.

SRO has a large impact on the defect evolution and mechanical properties in HEAs (Gupta et al., 2022b; Zhang et al., 2023a), the equivalence of the ion irradiation experiment with the long-term reactor neutron irradiation needs to be re-evaluated.

Although the approach of MC+MD method has been commonly used to study the equilibrium SRO state at a given annealing temperature, the recent finding based on kinetic simulations of vacancy diffusion through neural network-based KMC suggests that the SRO structures can differ from those obtained using the MC+MD method when considering the kinetic process (Xing et al., 2023). In contrast to the trend observed in the MC+MD method where the degree of SRO increases with deceasing temperature, there is a critical temperature at which the degree of B2 structure is maximum in the NbMoTa alloy. This is mainly because low-barrier transition states dominate lattice diffusion and restrict the nucleation of ordering structure at low temperature, although such structures are thermodynamically more stable. Therefore, it is of great interest to evaluate the diffusion kinetics on the degree of SRO at equilibrium. With the current lattice KMC simulations, such investigation would be impractical due to limitations in spatial and time scales. Machine learning-based methods, such as neural networks, offer promising approaches to extend the simulation scale, enabling more consistent simulations of the final SRO states (Xing et al., 2023). Recent studies have demonstrated that by parameterizing the local complex environment of the diffusion process with machine-learning approaches (Fan et al., 2022; Xu et al., 2023, 2022), the vacancy migration energy can be determined with great accuracy, compared to the NEB or middle-point method, while extending the time and spatial scales by several orders of magnitude. This is beneficial for studying ordered structures of larger dimensions and extending the time period to approach experimental conditions.

5. Conclusions

The evolution of the SRO structure in NiCoFeCrMn under irradiation including both the destruction and recovery processes has been studied by a multiscale approach, where the destruction process is modeled by cascade overlapping MD simulations and the recovery process induced by vacancy-mediated diffusion is modeled by means of kMC simulations. The SRO destruction rate is highly correlated to the number of replacement-per-atom, showing a universal law regardless of the PKA energy. The difference of SRO destruction rate among various element pairs is relatively small compared to that of SRO recovery rate. The defect structure has minor impact on the SRO destruction process. For the vacancy-induced SRO recovery process, Mn is the fast diffusion species and Mn-related SRO structure has the fastest recovery rate, while the recovery rates of Cr-Cr and other element pairs exhibit a comparatively slower trend. Under continuous irradiation, the steady-state SRO structure may be far away from the thermodynamic equilibrium state depending on the irradiation conditions, such as dose rate and temperature. Due to the difference between ion irradiation experiments and reactor conditions, it is necessary to evaluate the SRO evolution and the corresponding changes in defect evolution and mechanical properties in HEAs under reactor in-service conditions. The unsymmetrical destruction and recovery of the SRO structures under irradiation implies a novel routine to precisely modulate the local material properties via irradiation.

CRediT authorship contribution statement

Yundi Zhou: Data curation, Investigation, Formal analysis, Writing – original draft. **Tan Shi:** Conceptualization, Methodology, Writing – original draft, Writing – review & editing. **Jing Li:** Visualization, Investigation. **Lu Wu:** Visualization, Investigation. **Qing Peng:** Conceptualization, Software, Validation, Visualization, Writing – review & editing. **Chenyang Lu:** Funding acquisition, Resources, Supervision, Validation, Writing – review & editing.

Declaration of Competing Interest

The authors declare that they have no known competing financial interests or personal relationships that could have appeared to influence the work reported in this paper.

Data availability

Data will be made available on request.

Acknowledgement

This work was supported by the National Natural Science Foundation of China (grant nos 12075179, 12105219, and 12272378), National Key Research and Development Program of China (Grant No. 2019YFA0209900), the China Postdoctoral Science Foundation (Grant No. 2021M702583), the Innovative Scientific Program of China National Nuclear Corporation, High-level Innovation Research Institute Program of Guangdong Province (Grant No. 2020B0909010003), and the LiYing Program of the Institute of Mechanics, Chinese Academy of Sciences (Grant No. E1Z1011001), the Fundamental Research Funds for the Central Universities.

Supplementary materials

Supplementary material associated with this article can be found, in the online version, at doi:10.1016/j.ijplas.2023.103768.

References

Arkoub, H., Jin, M., 2023. Impact of chemical short-range order on radiation damage in Fe-Ni-Cr alloys. Scr. Mater. 229.
Averback, R.S., Bellon, P., Dillon, S.J., 2021. Phase evolution in driven alloys: an overview on compositional patterning. J. Nucl. Mater. 553.
Boleininger, M., Mason, D.R., Sand, A.E., Dudarev, S.L., 2023. Microstructure of a heavily irradiated metal exposed to a spectrum of atomic recoils. Sci. Rep. 13, 1684.
Butler, E.P., 2006. The effects of electron irradiation on the kinetics of order-disorder transformations. Radiat. Eff. 42, 17–22.
Chen, S., Aitken, Z.H., Pattamatta, S., Wu, Z., Yu, Z.G., Banerjee, R., Srolovitz, D.J., Liaw, P.K., Zhang, Y.-W., 2021a. Chemical-affinity disparity and exclusivity drive atomic segregation, short-range ordering, and cluster formation in high-entropy alloys. Acta Mater. 206.
Chen, W.-Y., Poplawsky, J.D., Chen, Y., Guo, W., Yeh, J.-W., 2020. Irradiation-induced segregation at dislocation loops in CoCrFeMnNi high entropy alloy. Materialia 14.
Chen, X., Wang, Q., Cheng, Z., Zhu, M., Zhou, H., Jiang, P., Zhou, L., Xue, Q., Yuan, F., Zhu, J., Wu, X., Ma, E., 2021b. Direct observation of chemical short-range order in a medium-entropy alloy. Nature 592, 712–716.
Chen, X., Yuan, F., Zhou, H., Wu, X., 2022. Structure motif of chemical short-range order in a medium-entropy alloy. Mater. Res. Lett. 10, 149–155.
Choi, W.M., Jo, Y.H., Sohn, S.S., Lee, S., Lee, B.-J., 2018. Understanding the physical metallurgy of the CoCrFeMnNi high-entropy alloy: an atomistic simulation study. NPJ Comput. Mater. 4.
Cowley, J.M., 1960. Short- and long-range order parameters in disordered solid solutions. Phys. Rev. 120, 1648–1657.
Demange, G., Lunéville, L., Pontikis, V., Simeone, D., 2017. Prediction of irradiation induced microstructures using a multiscale method coupling atomistic and phase field modeling: application to the AgCu model alloy. J. Appl. Phys. 121.
Ding, J., Yu, Q., Asta, M., Ritchie, R.O., 2018. Tunable stacking fault energies by tailoring local chemical order in CrCoNi medium-entropy alloys. Proc. Natl Acad. Sci. 115, 8919–8924.
Ding, Q., Zhang, Y., Chen, X., Fu, X., Chen, D., Chen, S., Gu, L., Wei, F., Bei, H., Gao, Y., 2019a. Tuning element distribution, structure and properties by composition in high-entropy alloys. Nature 574, 223–227.
Ding, Q., Zhang, Y., Chen, X., Fu, X., Chen, D., Chen, S., Gu, L., Wei, F., Bei, H., Gao, Y., Wen, M., Li, J., Zhang, Z., Zhu, T., Ritchie, R.O., Yu, Q., 2019b. Tuning element distribution, structure and properties by composition in high-entropy alloys. Nature 574, 223–227.
Du, J.-P., Yu, P., Shinzato, S., Meng, F.-S., Sato, Y., Li, Y., Fan, Y., Ogata, S., 2022. Chemical domain structure and its formation kinetics in CrCoNi medium-entropy alloy. Acta Mater. 240.
Enrique, R.A., Bellon, P., 2000. Compositional patterning in systems driven by competing dynamics of different length scale. Phys. Rev. Lett. 84, 2885.
Fan, Z., Xing, B., Cao, P., 2022. Predicting path-dependent diffusion barrier spectra in vast compositional space of multi-principal element alloys via convolutional neural networks. Acta Mater. 237.
Feng, X.B., Zhang, J.Y., Wang, Y.Q., Hou, Z.Q., Wu, K., Liu, G., Sun, J., 2017. Size effects on the mechanical properties of nanocrystalline NbMoTaW refractory high entropy alloy thin films. Int. J. Plast. 95, 264–277.
Fu, Y., Li, J., Luo, H., Du, C., Li, X., 2021. Recent advances on environmental corrosion behavior and mechanism of high-entropy alloys. J. Mater. Sci. Technol. 80, 217–233.
Gao, F., Bacon, D., Calder, A., Flewitt, P., Lewis, T., 1996. Computer simulation study of cascade overlap effects in α-iron. J. Nucl. Mater. 230, 47–56.
Granberg, F., Nordlund, K., Ullah, M.W., Jin, K., Lu, C., Bei, H., Wang, L.M., Djurabekova, F., Weber, W.J., Zhang, Y., 2016. Mechanism of radiation damage reduction in equiatomic multicomponent single phase alloys. Phys. Rev. Lett. 116.
Gupta, A., Jian, W.-R., Xu, S., Beyerlein, I.J., Tucker, G.J., 2022a. On the deformation behavior of CoCrNi medium entropy alloys: unraveling mechanistic competition. Int. J. Plast. 159.
Gupta, A., Jian, W.-R., Xu, S., Beyerlein, I.J., Tucker, G.J., 2022b. On the deformation behavior of CoCrNi medium entropy alloys: unraveling mechanistic competition. Int. J. Plast. 159, 103442.
Kamboj, A., Marquis, E.A., 2022. Effect of dose rate on the phase stability of a CrFeNiMn alloy. Scr. Mater. 215.
Ke, J.-H., Reese, E.R., Marquis, E.A., Odette, G.R., Morgan, D., 2019. Flux effects in precipitation under irradiation – Simulation of Fe-Cr alloys. Acta Mater. 164, 586–601.
Koch, L., Granberg, F., Brink, T., Utt, D., Albe, K., Djurabekova, F., Nordlund, K., 2017. Local segregation versus irradiation effects in high-entropy alloys: steady-state conditions in a driven system. J. Appl. Phys. 122.
Kozlov, A.V., 2009. Dependence of the concentration of point defects in the ChS-68 austenitic steel on the rate of their generation and temperature upon neutron irradiation. Phys. Met. Metall. 107, 534–541.

Kumar, N.A.P.K., Li, C., Leonard, K.J., Bei, H., Zinkle, S.J., 2016. Microstructural stability and mechanical behavior of FeNiMnCr high entropy alloy under ion irradiation. Acta Mater. 113, 230–244.
Levo, E., Granberg, F., Fridlund, C., Nordlund, K., Djurabekova, F., 2017. Radiation damage buildup and dislocation evolution in Ni and equiatomic multicomponent Ni-based alloys. J. Nucl. Mater. 490, 323–332.
Li, C., Hu, X., Yang, T., Kumar, N.A.P.K., Wirth, B.D., Zinkle, S.J., 2019a. Neutron irradiation response of a Co-free high entropy alloy. J. Nucl. Mater. 527.
Li, Q.J., Sheng, H., Ma, E., 2019b. Strengthening in multi-principal element alloys with local-chemical-order roughened dislocation pathways. Nat. Commun. 10, 3563.
Li, Y., Du, J.-P., Yu, P., Li, R., Shinzato, S., Peng, Q., Ogata, S., 2022. Chemical ordering effect on the radiation resistance of a CoNiCrFeMn high-entropy alloy. Comput. Mater. Sci. 214.
Li, TX, Miao, JW, Guo, EY, Huang, H, Wang, J, Lu, YP, Wang, TM, Cao, ZQ, Li, TJ, 2021. Tungsten-containing high-entropy alloys: a focused review of manufacturing routes, phase selection, mechanical properties, and irradiation resistance properties. Tungsten 3 (2), 181–196.
Li, Y., Nutor, R.K., Zhao, Q., Zhang, X., Cao, Q., Sohn, S., Wang, X., Ding, S., Zhang, D., Zhou, H., 2023. Unraveling the deformation behavior of the Fe45Co25Ni10V20 high entropy alloy. Int. J. Plast., 103619
Li, Z., Pradeep, K.G., Deng, Y., Raabe, D., Tasan, C.C., 2016. Metastable high-entropy dual-phase alloys overcome the strength-ductility trade-off. Nature 534, 227–230.
Liu, L., Liu, X., Du, Q., Wang, H., Wu, Y., Jiang, S., Lu, Z., 2022. Local chemical ordering and its impact on radiation damage behavior of multi-principal element alloys. J. Mater. Sci. Technol.
Lu, C., Niu, L., Chen, N., Jin, K., Yang, T., Xiu, P., Zhang, Y., Gao, F., Bei, H., Shi, S., 2016. Enhancing radiation tolerance by controlling defect mobility and migration pathways in multicomponent single-phase alloys. Nat. Commun. 7, 1–8.
Lu, C.Y., Yang, T.N., Jin, K., Gao, N., Xiu, P.Y., Zhang, Y.W., Gao, F., Bei, H.B., Weber, W.J., Sun, K., Dong, Y., Wang, L.M., 2017. Radiation-induced segregation on defect clusters in single-phase concentrated solid-solution alloys. Acta Mater. 127, 98–107.
Martin, G., 1984. Phase stability under irradiation: ballistic effects. Phys. Rev. B 30, 1424–1436.
Nordlund, K., Zinkle, S.J., Sand, A.E., Granberg, F., Averback, R.S., Stoller, R., Suzudo, T., Malerba, L., Banhart, F., Weber, W.J., Willaime, F., Dudarev, S.L., Simeone, D., 2018. Improving atomic displacement and replacement calculations with physically realistic damage models. Nat. Commun. 9, 1084.
Norgett, M., Robinson, M., Torrens, I.M., 1975. A proposed method of calculating displacement dose rates. Nucl. Eng. Des. 33, 50–54.
Otto, F., Dlouhý, A., Pradeep, K.G., Kuběnová, M., Raabe, D., Eggeler, G., George, E.P., 2016. Decomposition of the single-phase high-entropy alloy CrMnFeCoNi after prolonged anneals at intermediate temperatures. Acta Mater. 112, 40–52.
Peng, Q., Meng, F., Yang, Y., Lu, C., Deng, H., Wang, L., De, S., Gao, F., 2018. Shockwave generates < 100 >dislocation loops in bcc iron. Nat. Commun. 9.
Plimpton, S., 1995. Fast parallel algorithms for short-range molecular dynamics. J. Comput. Phys. 117, 1–19.
Shen, Z., Du, J.-P., Shinzato, S., Sato, Y., Yu, P., Ogata, S., 2021. Kinetic Monte Carlo simulation framework for chemical short-range order formation kinetics in a multi-principal-element alloy. Comput. Mater. Sci. 198.
Shi, T., Lei, P.-H., Yan, X., Li, J., Zhou, Y.-D., Wang, Y.-P., Su, Z.-X., Dou, Y.-K., He, X.-F., Yun, D., 2021. Current development of body-centered cubic high-entropy alloys for nuclear applications. Tungsten 3, 197–217.
Shi, T., Lyu, S., Su, Z., Wang, Y., Qiu, X., Sun, D., Xin, Y., Li, W., Cao, J., Peng, Q., 2023a. Spatial inhomogeneity of point defect properties in refractory multi-principal element alloy with short-range order: a first-principles study. J. Appl. Phys. 133.
Shi, T., Qiu, X., Zhou, Y., Lyu, S., Li, J., Sun, D., Peng, Q., Xin, Y., Lu, C., 2023b. Unconventional energetics of small vacancy clusters in BCC high-entropy alloy Nb0.75ZrTiV0.5. J. Mater. Sci. Technol. 146, 61–71.
Shi, T., Su, Z., Li, J., Liu, C., Yang, J., He, X., Yun, D., Peng, Q., Lu, C., 2022. Distinct point defect behaviours in body-centered cubic medium-entropy alloy NbZrTi induced by severe lattice distortion. Acta Mater. 229.
Sickafus, K.E., Kotomin, E.A., Uberuaga, B.P., 2007. Radiation Effects in Solids. Springer Science & Business Media.
Stukowski, A., 2010. Visualization and analysis of atomistic simulation data with OVITO–the Open Visualization Tool. Modell. Simul. Mater. Sci. Eng. 18.
Stukowski, A., 2012. Structure identification methods for atomistic simulations of crystalline materials. Modell. Simul. Mater. Sci. Eng. 20.
Su, Z., Shi, T., Shen, H., Jiang, L., Wu, L., Song, M., Li, Z., Wang, S., Lu, C., 2022a. Radiation-assisted chemical short-range order formation in high-entropy alloys. Scr. Mater. 212.
Su, Z., Shi, T., Yang, J., Shen, H., Li, Z., Wang, S., Ran, G., Lu, C., 2022b. The effect of interstitial carbon atoms on defect evolution in high entropy alloys under helium irradiation. Acta Mater. 233.
Sun, S., Zai, W., Chen, Y., Zhao, L., Sun, G., Hu, J., Han, S., Lian, J., 2022. Effects of cold-rolling and subsequent annealing on the nano-mechanical and creep behaviors of CrCoNi medium-entropy alloy. Mater. Sci. Eng. 839, 142802.
Tsai, K.Y., Tsai, M.H., Yeh, J.W., 2013. Sluggish diffusion in Co–Cr–Fe–Mn–Ni high-entropy alloys. Acta Mater. 61, 4887–4897.
Was, G.S., 2016. Fundamentals of radiation materials science: Metals and alloys. Springer.
Wharry, J.P., Was, G.S., 2013. A systematic study of radiation-induced segregation in ferritic–martensitic alloys. J. Nucl. Mater. 442, 7–16.
Xing, B., Rupert, T.J., Pan, X., Cao, P., 2023. Neural network kinetics: diffusion multiplicity and b2 ordering in compositionally complex alloys. arXiv preprint arXiv: 2304.02957.
Xing, B., Wang, X., Bowman, W.J., Cao, P., 2022. Short-range order localizing diffusion in multi-principal element alloys. Scr. Mater. 210.
Xu, B., Ma, S., Huang, S., Zhang, J., Xiong, Y., Fu, H., Xiang, X., Zhao, S., 2023. Influence of short-range order on diffusion in multiprincipal element alloys from long-time atomistic simulations. Phys. Rev. Materials 7.
Xu, B., Zhang, J., Ma, S., Xiong, Y., Huang, S., Kai, J.J., Zhao, S., 2022. Revealing the crucial role of rough energy landscape on self-diffusion in high-entropy alloys based on machine learning and kinetic Monte Carlo. Acta Mater. 234.
Yeh, J.W., Chen, S.K., Lin, S.J., Gan, J.Y., Chin, T.S., Shun, T.T., Tsau, C.H., Chang, S.Y., 2004. Nanostructured high-entropy alloys with multiple principal elements: novel alloy design concepts and outcomes. Adv. Eng. Mater. 6, 299–303.
Yoshizaki, H., Hashimoto, A., Kaneno, Y., Semboshi, S., Hori, F., Saitoh, Y., Iwase, A., 2015. Energetic ion beam induced crystal phase transformation and resulting hardness change in Ni3Al intermetallic compound. Nucl. Instrum. Methods Phys. Res., Sect. B 354, 287–291.
Zhang, H.K., Yao, Z., Kirk, M.A., Daymond, M.R., 2014. Stability of Ni3(Al, Ti) gamma prime precipitates in a nickel-based superalloy inconel X-750 under heavy ion irradiation. Metall. Mater. Trans. A 45, 3422–3428.
Zhang, J., He, Q., Li, J., Yang, Y., 2021. Chemical fluctuation enabling strength-plasticity synergy in metastable single-phase high entropy alloy film with gigapascal yield strength. Int. J. Plast. 139, 102951.
Zhang, R., Zhao, S., Ding, J., Chong, Y., Jia, T., Ophus, C., Asta, M., Ritchie, R.O., Minor, A.M., 2020a. Short-range order and its impact on the CrCoNi medium-entropy alloy. Nature 581, 283–287.
Zhang, T., Ma, S., Zhao, D., Wu, Y., Zhang, Y., Wang, Z., Qiao, J., 2020b. Simultaneous enhancement of strength and ductility in a NiCoCrFe high-entropy alloy upon dynamic tension: micromechanism and constitutive modeling. Int. J. Plast. 124, 226–246.
Zhang, X., Yan, J., Chen, Y.-H., Kevorkyants, R., Wen, T., Sun, X., Hu, A., Huang, J., 2023a. Effects of lattice distortion and chemical short-range ordering on the incipient behavior of Ti-based multi-principal element alloys: MD simulations and DFT calculations. Int. J. Plast. 166, 103643.
Zhang, Y., Stocks, G.M., Jin, K., Lu, C., Bei, H., Sales, B.C., Wang, L., Béland, L.K., Stoller, R.E., Samolyuk, G.D., 2015. Influence of chemical disorder on energy dissipation and defect evolution in concentrated solid solution alloys. Nat. Commun. 6, 1–9.
Zhang, Z., Su, Z., Zhang, B., Yu, Q., Ding, J., Shi, T., Lu, C., Ritchie, R.O., Ma, E., 2023b. Effect of local chemical order on the irradiation-induced defect evolution in CrCoNi medium-entropy alloy. Proc. Natl Acad. Sci. 120, e2218673120.
Zhao, S., 2021. Role of chemical disorder and local ordering on defect evolution in high-entropy alloys. Phys. Rev. Materials 5.
Zhao, S., Egami, T., Stocks, G.M., Zhang, Y., 2018. Effect of d electrons on defect properties in equiatomic NiCoCr and NiCoFeCr concentrated solid solution alloys. Phys. Rev. Materials 2, 013602.

Zhao, Y., Bhattacharya, A., Pareige, C., Massey, C., Zhu, P., Poplawsky, J.D., Henry, J., Zinkle, S.J., 2022. Effect of heavy ion irradiation dose rate and temperature on α' precipitation in high purity Fe-18 %Cr alloy. Acta Mater. 231.
Ziegler, J.F., Biersack, J.P., 1985. The stopping and range of ions in matter. Treatise on Heavy-Ion Science. Springer, pp. 93–129.
Zinkle, S.J., Was, G.S., 2013. Materials challenges in nuclear energy. Acta Mater. 61, 735–758.
Ziya, A.B., Abbas, T., Wang, X., 2003. Isothermal relaxation of short-range order in the ternary Au25Ag25Pd50 alloy. Scr. Mater. 49, 453–457.